MICROWAVE AND OPTICAL TECHNOLOGY LETTERS

VOLUME 63 / NUMBER 3 MARCH 2021

EDITOR
Wenquan Che
South China University of Technology
School of Electronic and
Information Engineering

MICROWAVE AND OPTICAL TECHNOLOGY LETTERS ISSN: 0895-2477 (Print); ISSN 1098-2760 (Online) is published monthly by Wiley Periodicals LLC, a Wiley Company, 111 River Street, Hoboken, NJ 07030-5774. Periodical Postage Paid at Hoboken, NJ and additional offices.

Postmaster: Send all address changes to MICROWAVE AND OPTICAL TECHNOLOGY LETTERS, Wiley Periodicals LLC, C/O The Sheridan Press, PO Box 465, Hanover, PA 17331 USA.

Aims and Scope

MICROWAVE AND OPTICAL TECHNOLOGY LETTERS provides quick publication (three- to six-month turnaround) of the most recent findings and achievements in high frequency technology, from RF to optical spectrum. The journal publishes original short papers and letters on theoretical, applied, and system results in the following areas:

RF, Microwave, and Millimeter Waves
Antennas and Propagation
Submillimeter-Wave and Infrared Technology
Optical Engineering

All papers are subject to peer review before publication.

Information for subscribers: MICROWAVE AND OPTICAL TECHNOLOGY LETTERS is published in 12 issues per year. Institutional subscription prices for 2021 are: Print & Online US$7096 (US), US$7512 (Rest of World), €4849 (Europe), £3837 (UK). Prices are exclusive of tax. Asia-Pacific GST, Canadian GST/HST and European VAT will be applied at the appropriate rates. For more information on current tax rates, please go to www.wileyonlinelibrary.com/tax-vat. The price includes online access to the current and all online back files to January 1st 2017, where available. For other pricing options, including access information and terms and conditions, please visit www.wileyonlinelibrary.com/access.

Delivery Terms and Legal Title: Where the subscription price includes print issues and delivery is to the recipient's address, delivery terms are Delivered at Place (DAP); the recipient is responsible for paying any import duty or taxes. Title to all issues transfers FOB our shipping point, freight prepaid. We will endeavour to fulfill claims for missing or damaged copies within six months of publication, within our reasonable discretion and subject to availability.

Journal Customer Services: For ordering information, claims and any enquiry concerning your journal subscription please go to www.wileycustomerhelp.com/ask or contact your nearest office.
Americas: Email: cs-journals@wiley.com; Tel: +1 781 388 8598 or +1 800 835 6770 (Toll free in the USA & Canada).
Europe, Middle East and Africa: Email: cs-journals@wiley.com; Tel: +44 (0) 1865 778315.
Asia Pacific: Email: cs-journals@wiley.com; Tel: +65 6511 8000.
Japan: For Japanese speaking support, Email: cs-japan@wiley.com.
Visit our Online Customer Help available in 7 languages at www.wileycustomerhelp.com/ask
Back issues: Single issues from current and recent volumes are available at the current single issue price from cs-journals@wiley.com. Earlier issues may be obtained from Periodicals Service Company, 351 Fairview Avenue - Ste 300, Hudson, NY 12534, USA. Tel: +1 518 822-9300, Fax: +1 518 822-9305, Email: psc@periodicals.com
Author Reprints (50–500 copies): Order online: http://www.sheridanreprints.com/order-form.html; Email: Chris.Jones@sheridan.com
Manuscripts should be submitted online at: https://mc.manuscriptcentral.com/mop
Wiley's Corporate Citizenship initiative seeks to address the environmental, social, economic, and ethical challenges faced in our business and which are important to our diverse stakeholder groups. Since launching the initiative, we have focused on sharing our content with those in need, enchancing community philanthropy, reducing our carbon impact, creating global guidelines and best practices for paper use, establishing a vendor code of ethics, and engaging our colleagues and other stakeholders in our efforts.
Other correspondence should be addressed to: MICROWAVE AND OPTICAL TECHNOLOGY LETTERS, Publisher, c/o John Wiley & Sons, Inc., 111 River Street, Hoboken, NJ 07030. For submission instructions, subscription, and all other information visit: wileyonlinelibrary.com/journal/mop

View this journal online at wileyonlinelibrary.com/journal/mop
Printed in the USA by The Sheridan Group.
Production Editor: Kamatchi Dilli (email: jrnlprod_MOP@wiley.com).

This paper meets the requirements of ANSI/NISO Z39, 48-1992 (Permancence of Paper). ∞

MICROWAVE AND OPTICAL TECHNOLOGY LETTERS

VOLUME 63 / NUMBER 3 **MARCH 2021**

RESEARCH ARTICLES

MICROWAVE AND OPTICAL TECHNOLOGY LETTERS

March 2021

Previous Issue | Next Issue

GO TO SECTION

Export Citation(s)

ISSUE INFORMATION

RESEARCH ARTICLES

Received: 14 September 2020
DOI: 10.1002/mop.32696

RESEARCH ARTICLE

A highly independent and controllable dual-band bandpass filter based on source-load coupling with stub-block isolation structure

Yus Rama Denny[1] | **Teguh Firmansyah**[2]

[1]Department of Physics Education, Universitas Sultan Ageng Tirtayasa, Serang, Banten, Indonesia

[2]Department of Electrical Engineering, Universitas Sultan Ageng Tirtayasa, Cilegon, Banten, Indonesia

Correspondence
Yus Rama Denny, Department of Physics Education, Universitas Sultan Ageng Tirtayasa, Serang, Banten, 42118, Indonesia.
Email: yusramadenny@untirta.ac.id;

Teguh Firmansyah, Department of Electrical Engineering, Universitas Sultan Ageng Tirtayasa, Cilegon, Banten, 42435, Indonesia.
Email: teguhfirmansyah@untirta.ac.id

Funding information
Ministry of Education and culture, Indonesian Government, Grant/Award Number: 2020-2021

Abstract

The main problem of dual-band bandpass filter (BPF) structures is to control each passband performance individually, separately, and independently. This Letter is proposed a dual-band BPF based on a source-load coupling structure with stub-block isolation to overcome the problem. The lower band resonator structure is placed on the top side, while the upper band resonator is placed at the bottom side, with the source-load (SL) coupling structure in the middle. An additional stub-block isolation structure is added to the center of the SL coupling structure. As a result, we have successfully designed an independent dual-band bandpass filter with highly controllable working frequency/frequency center (f_c), bandwidth (BW), reflection coefficient (S_{11}), and isolation (ISO) between the passbands. The proposed dual-band BPF was fabricated on an RT/Duroid 5880 substrate. Furthermore, this dual-band BPF achieved an insertion loss/fractional bandwidth of 0.48 dB/7.71% and 0.35 dB/12.37% at 1.82 and 2.58 GHz, respectively. The good agreement between the simulated and measured results validates the proposed method.

KEYWORDS
controllable dual-band BPF, source-load coupling, stub-block isolation

1 | INTRODUCTION

A highly flexible RF device must be supported by a high-performance bandpass filter (BPF) that can be controlled. This requirement has motivated many researchers to produce BPFs with controllable performance.[1] Several methods have been proposed to control the frequency passband, such as the stepped impedance ring resonator (SIRR) with shorted stubs,[2] defected and irregular stepped-impedance resonators (DI-SIRs),[3] multilayer resonator,[4] loop resonator,[5] cross resonator,[6] substrate-integrated waveguide (SIW) cavities,[7] and half-mode substrate integrated waveguide (HMSIW).[8] Furthermore, to increase the isolation, some researchers have proposed a circular resonator[9] and a ring resonator. Moreover, a quasi-elliptical waveguide resonator was proposed by Reference 10 to control the frequency and bandwidth. However, none of the proposed methods has a controllable performance frequency, bandwidth, reflection coefficient, and isolation simultaneously.

In this Letter, a dual-band BPF based on a source-load coupling structure is proposed, as shown in Figure 1A. It is clearly distinct from the microstrip structure used in References 1-11. The topology of the coupling structure is given in Figure 1B. Furthermore, M_{MN} denotes the coupling matrix values between two resonators for ($M = S, 1, 2, L$ and $N = S, 1, 2, L$), can be derived as follows:

$$M_{MN} = \begin{pmatrix} 0 & 0.307 & 0 & -0.389 & 0 & 1.000 \\ 0.307 & 0.819 & 0.080 & 0 & 0 & 0 \\ 0 & 0.080 & -0.579 & 0 & 0 & 0.008 \\ -0.389 & 0 & 0 & -25.95 & -66.122 & 0 \\ 0 & 0 & 0 & -66.122 & -169.205 & -0.116 \\ 1.000 & 0 & 0.008 & 0 & -0.116 & 0 \end{pmatrix}$$

The coefficients of the coupling matrix are taken from the optimization process. By using this structure, the frequency, bandwidth, reflection coefficient, and isolation in each passband can be adjusted individually with

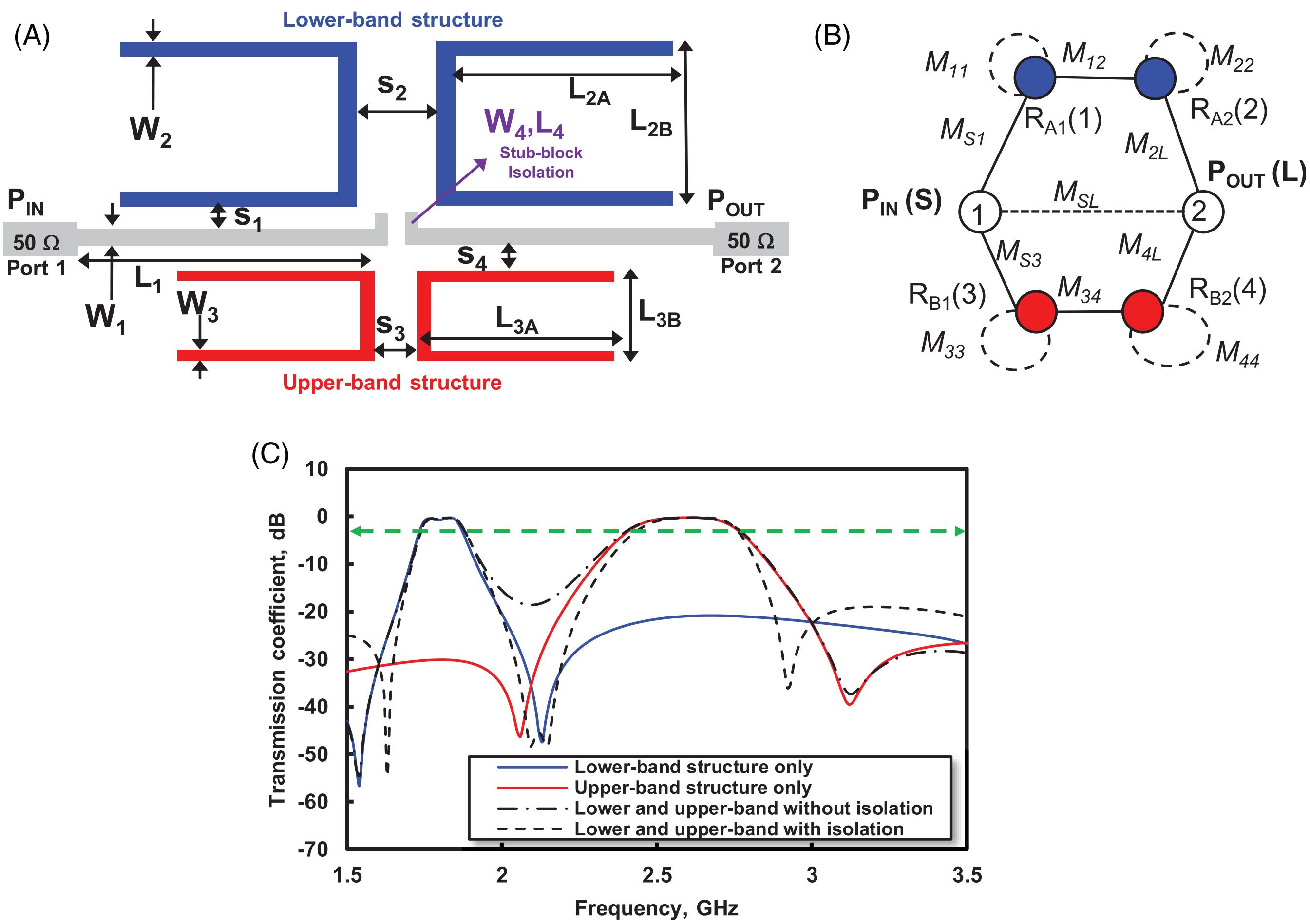

FIGURE 1 A, proposed dualband BPF with a source-load coupling structure and stub-block isolation; B, topology of the coupling structure; and C, the dualband BPF response strategy [Color figure can be viewed at wileyonlinelibrary.com]

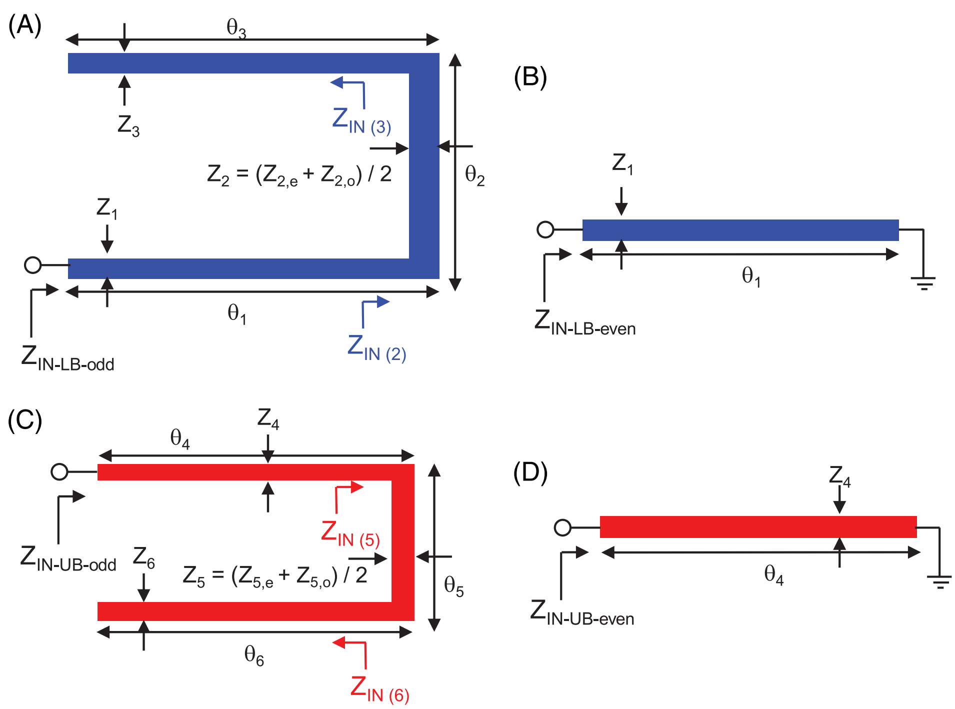

FIGURE 2 A, Odd-mode structure lower band; B, even-mode structure lower band; C, Odd-mode structure upper band; and D, even-mode structure upper band [Color figure can be viewed at wileyonlinelibrary.com]

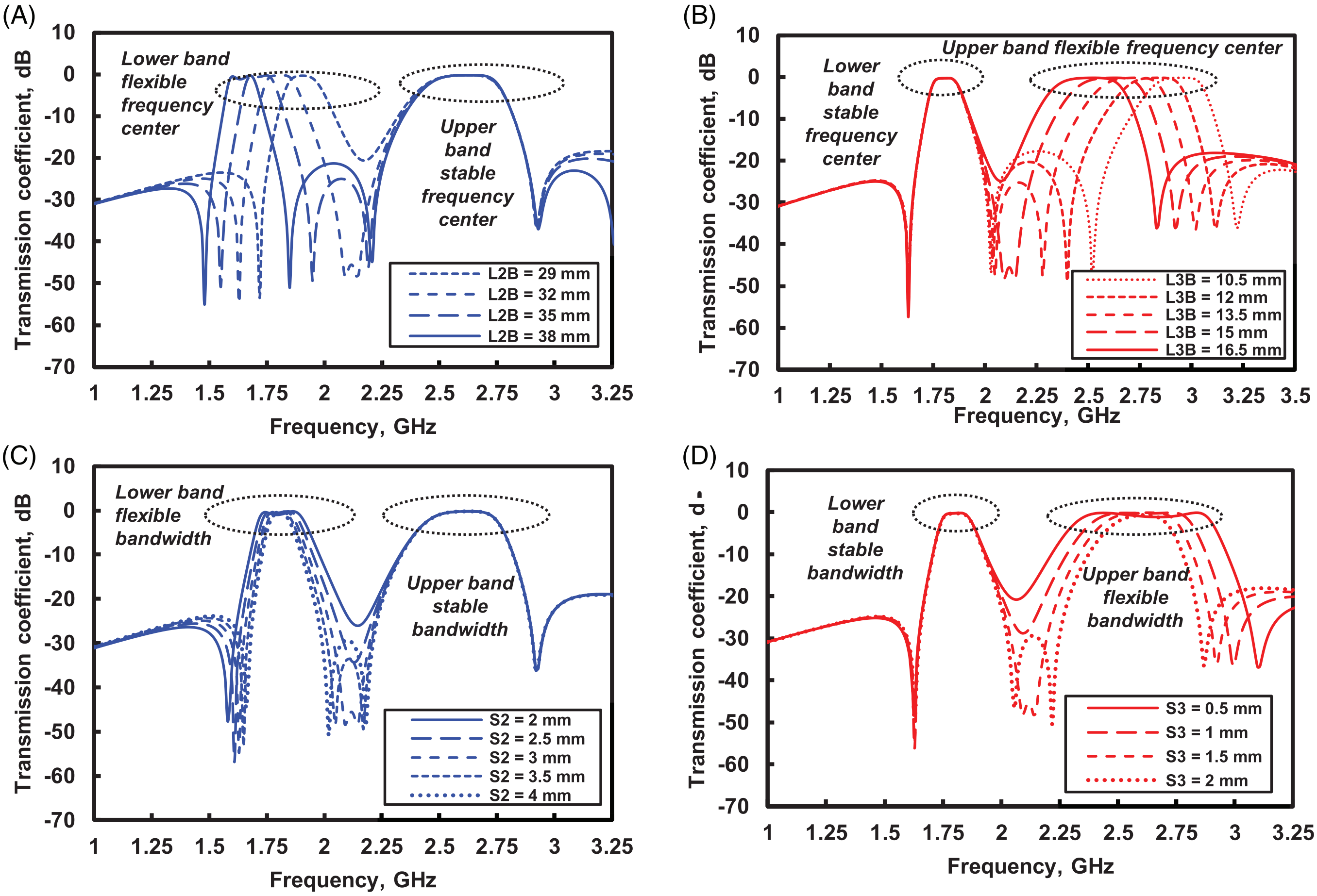

FIGURE 3 A, Band pass frequency of the lower band for various lengths L_{2B}; B, band pass frequency of the upper band for various lengths L_{3B}; C, bandwidth characteristics of the lower band for various gaps S_2; and D, bandwidth characteristics of the upper band for various gaps S_3 [Color figure can be viewed at wileyonlinelibrary.com]

convenience and robustness. The proposed method is validated by the good agreement between the simulated and measured results.

2 | DUAL-BAND BPF BASED ON SOURCE-LOAD COUPLING WITH STUB-BLOCK ISOLATION

The proposed dual-band BPF is constructed by using four important segments, that is, a source-load coupling structure, a lower band resonator, an upper band resonator, and an additional isolation structure. The source-load (P_{IN} and P_{OUT}) coupling structure is positioned in the middle, where (W_1, L_1) represent the width and length, respectively. Furthermore, the lower band resonators are placed at the top, constructed by a coupled-resonator (R_{A1} and R_{A2}) with the back-to-back position, where (W_2, L_{2A}, L_{2B}) represent the widths and lengths of the lower band resonator. Moreover, the upper band resonators are arranged at the bottom. They are composed of a coupled-resonator (R_{B1} and R_{B2}) with a back-to-back position, where (W_3, L_{3A}, L_{3B}) represent the widths and lengths of the upper band resonator. The additional isolation is added at the center, with (W_4, L_4) representing the width and length isolation structures, respectively. Furthermore, (S_1, S_2, S_3, S_4) represent the gaps between the source/load and lower band, intercoupled lower band, intercoupled upper band, and source/load and upper band, respectively.

Figure 1C shows the dual-band BPF response. If the lower band or upper band structures are applied separately, the transmission coefficient will respond separately. However, if they are combined, the interference between two passbands will increase. To reduce interference, the isolation structure should be added at the center. Furthermore, the odd-mode structure of lower band, even-mode structure of lower band, odd-mode structure of upper band, and even-mode structure of upper band are shown in Figure 2A-D, respectively. The value input impedance of odd-mode at lower band $Z_{IN\text{-}LB\text{-}odd}$ can be derived:

$$Z_{IN(3)} = -jZ_3\cot\theta_3 \tag{1}$$

$$Z_{IN(2)} = Z_2\frac{Z_{IN(3)} + jZ_2\tan\theta_2}{Z_2 + jZ_{IN(3)}\tan\theta_2} \tag{2}$$

$$Z_{IN-LB-odd} = Z_1\frac{Z_{IN(2)} + jZ_1\tan\theta_1}{Z_1 + jZ_{IN(2)}\tan\theta_1} \tag{3}$$

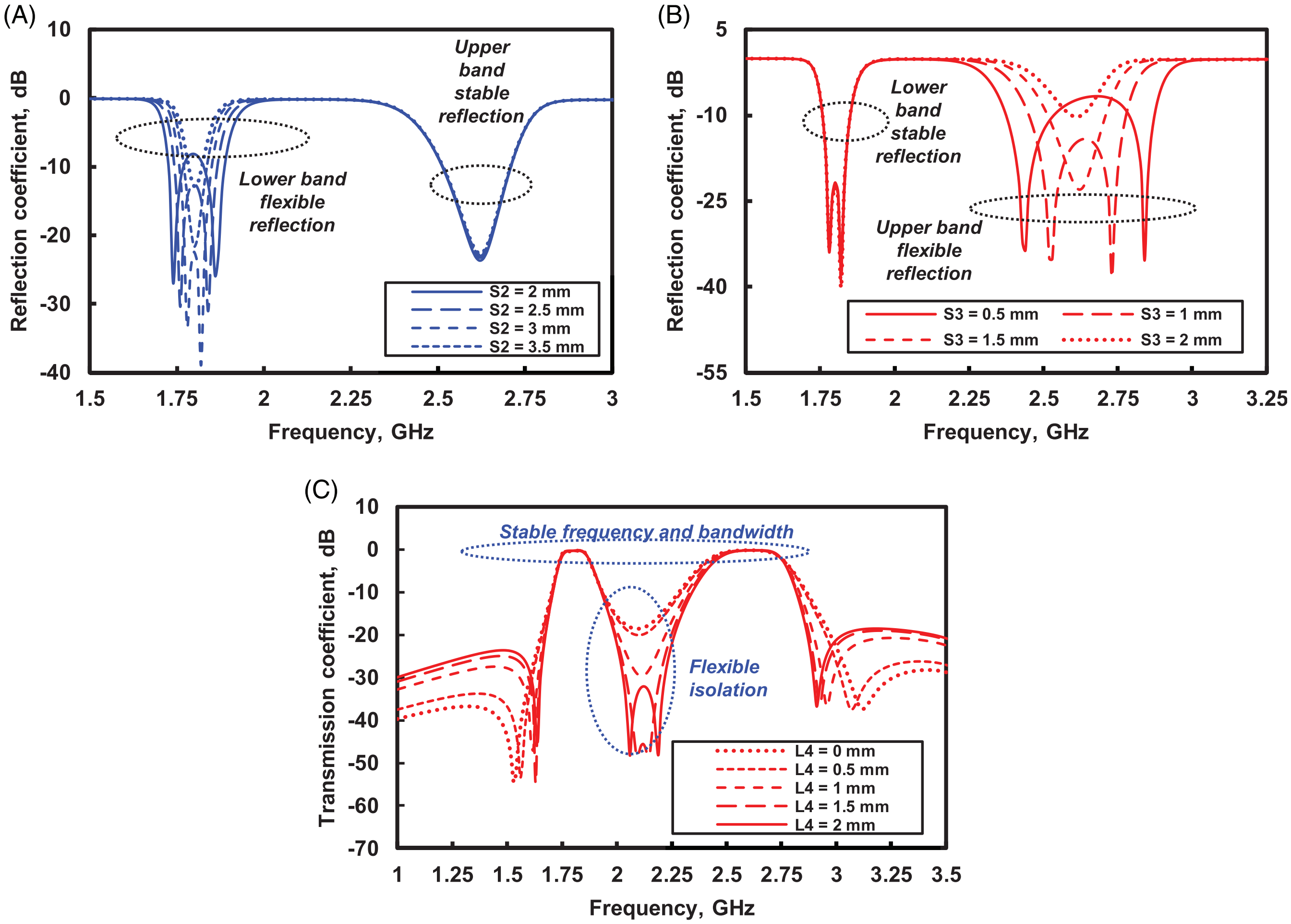

FIGURE 4 A, Reflection coef. Characteristics of the lower band for various gaps S_2; B, reflection coef. Characteristics of the upper band for various gaps S_3; and C, isolation characteristics for various lengths L_4 [Color figure can be viewed at wileyonlinelibrary.com]

Moreover, Equation (3) can also be expressed as:

$$Z_{IN-LB-odd} = Z_1 \frac{Z_2(-jZ_1\cot\theta_1 + jZ_2\tan\theta_2) + jZ_3\tan\theta_3(Z_2 + Z_1\cot\theta_1\tan\theta_2)}{Z_3Z_2 + Z_3Z_1\cot\theta_1\tan\theta_2 + Z_2Z_1\cot\theta_1\tan\theta_1 - Z_2^2\tan\theta_2\tan\theta_3} \quad (4)$$

with

$$Z_2 = \frac{Z_{2,e} + Z_{2,o}}{2} \quad (5)$$

The resonant can be derived from admittance condition $Y_{IN-LB-odd} = 0$ or impedance condition $Z_{IN-LB-odd} = \infty$,[1] or it has a denominator equal with zero.

$$Z_3\left(\frac{Z_{2,e} + Z_{2,o}}{2}\right) + Z_3Z_1\cot\theta_1\tan\theta_2 + Z_1\left(\frac{Z_{2,e} + Z_{2,o}}{2}\right)\cot\theta_1\tan\theta_1 - \left(\frac{Z_{2,e} + Z_{2,o}}{2}\right)^2\tan\theta_2\tan\theta_3 = 0 \quad (6)$$

Furthermore, the value input impedance of even-mode at lower band $Z_{IN\text{-}LB\text{-}even}$ can be derived:

$$Z_{IN-LB-even} = jZ_1\tan\theta_1 \quad (7)$$

Moreover, the value input impedance of odd-mode at upper band $Z_{IN\text{-}UB\text{-}odd}$ can be derived:

$$Z_{IN(6)} = -jZ_6\cot\theta_6 \quad (8)$$

$$Z_{IN(5)} = Z_5\frac{Z_{IN(6)} + jZ_5\tan\theta_5}{Z_5 + jZ_{IN(6)}\tan\theta_5} \quad (9)$$

$$Z_{IN-UB-odd} = Z_4\frac{Z_{IN(5)} + jZ_4\tan\theta_4}{Z_4 + jZ_{IN(5)}\tan\theta_4} \quad (10)$$

Equation (10) can also be derived as:

$$Z_{IN-UB-odd} = Z_4\frac{Z_5(-jZ_4\cot\theta_4 + jZ_5\tan\theta_5) + jZ_6\tan\theta_6(Z_5 + Z_4\cot\theta_4\tan\theta_5)}{Z_6Z_5 + Z_6Z_4\cot\theta_4\tan\theta_5 + Z_5Z_4\cot\theta_4\tan\theta_4 - Z_5^2\tan\theta_5\tan\theta_6} \quad (11)$$

with

$$Z_5 = \frac{Z_{5,e} + Z_{5,o}}{2} \quad (16)$$

The resonant can be derived from admittance condition $Y_{IN-UB-odd} = 0$ or impedance condition $Z_{IN-UB-odd} = \infty$,[1] or it has a denominator equal with zero.

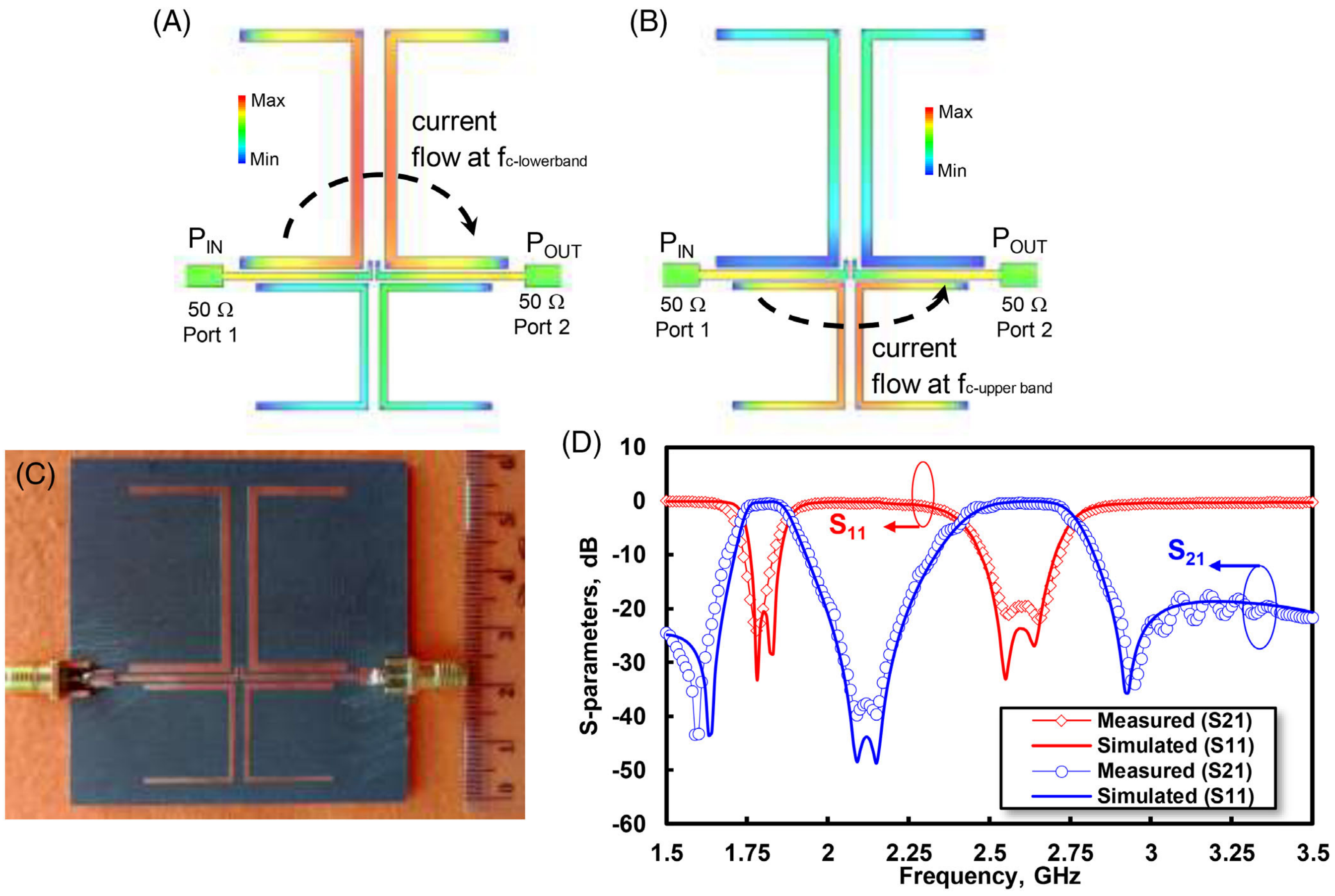

FIGURE 5 Current surface at A, lower band of $f_c = 1.82$ GHz; B, upper band of $f_c = 2.58$ GHz; and C, photograph of the proposed method; and D, comparison of simulated and measured result [Color figure can be viewed at wileyonlinelibrary.com]

$$Z_5\left(\frac{Z_{5,e}+Z_{5,o}}{2}\right)+Z_6Z_4\cot\theta_4\tan\theta_5 +Z_4\left(\frac{Z_{5,e}+Z_{5,o}}{2}\right)\cot\theta_4\tan\theta_4 -\left(\frac{Z_{5,e}+Z_{5,o}}{2}\right)^2\tan\theta_5\tan\theta_6=0 \tag{17}$$

Furthermore, the value input impedance of even-mode at upper band $Z_{IN\text{-}LB\text{-}even}$ can be derived:

$$Z_{IN-UB-even}=jZ_4\tan\theta_1 \tag{18}$$

with the impedance (Z_N) and electric length (θ_N).

3 | RESULTS AND DISCUSSION

Figure 3A,B show the relationship between the bandpass frequency/frequency center of the lower band response under various lengths L_{2B} and the bandpass frequency/frequency center of the upper band response under various lengths L_{3B}, respectively. The figures show that by increasing the dimension of $L_{2B,}$ the bandpass frequency of the lower band will gradually shift to a lower frequency, while the upper band will remain stable. Moreover, the bandpass frequency of the upper band will be shifted by various lengths L_{3B}, while the lower band will remain stable.

Moreover, Figure 3C, D show the relationship the bandwidth characteristics of the lower band for various gaps S_2, and the bandwidth characteristics of the upper band for various gaps S_3, respectively. Moreover, the bandwidth of each passband can be controlled individually and separately by varying the gaps S_2 and S_3. It can be seen that by increasing the gap S_2, the bandwidth of the lower band will become narrower and can be adjusted separately. Furthermore, by decreasing gap S_3, the bandwidth of the upper band only will increase.

Figure 4A-C show the reflection coefficient characteristics of the lower band for various gaps S_2, the reflection coefficient characteristics of the upper band for various gaps S_3, and the isolation characteristics for various lengths L_4, respectively. The reflection coefficient value of the lower band can be controlled separately by varying gap S_2 without any impact on the upper band. Moreover, the reflection coefficient value of the upper band can be adjusted individually by varying gap S_3. Furthermore, the isolation characteristics can be changed by varying the length L_4 without affecting the frequency passband or bandwidth of the lower band and

TABLE 1 Comparison with some previous dualband BPFs

Refs.	Freq (GHz)	Insertion loss (dB)	−3 dB FBW (%)	Independent and controllable			
				Freq	BW	Ref. coef	ISO
2	1.39/1.82	2.48/3.60	9.30/6.60	Yes	–	–	–
3	2.45/5.20	1.30/2.80	6.93/4.03	Yes	–	–	–
5	5.01/8.25	0.81/0.83	6.59/6.10	Yes	–	–	–
6	1.14/2.31	0.22/1.87	94.19/33.52	Yes	–	–	–
7	3.61/6.40	1.30/1.20	8.20/6.70	Yes	–	–	–
9	2.43/3.73	2.50/1.30	4.50/6.10	–	–	–	Yes
10	2.40/5.20	1.40/3.00	9.20/9.50	–	–	–	Yes
11	3.78/4.82	1.38/1.82	11.3/10.7	Yes	–	–	–
12	0.69/2.67	0.70/1.76	23.5/30.0	–	Yes	–	–
13	1.57/2.38	1.21/1.95	9.90/6.50	–	–	–	Yes
14	2.52/3.54	0.62/0.55	5.90/5.10	Yes	–	–	–
15	8.13/11.13	0.88/1.28	3.90/3.60	Yes	–	–	–
16	2.40/3.20	1.47/1.65	15.4/10.9	Yes	Yes	–	–
17	9.42/9.99	2.20/2.30	3.00/3.30	–	Yes	–	–
18	1.59/1.92	1.49/1.44	6.90/9.40	Yes	–	–	–
19	5.50/12.5	0.50/2.91	92.0/17.0	–	Yes	–	–
This study	1.82/2.58	0.48/0.35	7.71/12.37	Yes	Yes	Yes	Yes

Abbreviations: BW, bandwidth; FBW, fractional bandwidth; ISO, isolation.

upper band. Moreover, Figure 5A,B show the current surface at lower-band of f_c = 1.82 GHz and upper band of f_c = 2.58 GHz, respectively. It can be seen that at the lower band, the surface current flows at upper part of BPF. Meanwhile, the surface current flows at lower part of BPF at the upper band.

The proposed dual-band BPF was fabricated on an RT/Duroid 5880 substrate with a permittivity of 2.2 and a thickness of 1.575 mm. A momentum simulation produced by the Advanced Design System (ADS) was used to optimize the structure. Furthermore, the R&S ZVA67 VNA was used to measure the BPF performance. The dimensions were as follows (all in millimeters): W_1 = 1.0, W_2 = 1.5, W_3 = 1.0, W_4 = 0.5, L_1 = 10, L_{2A} = 15, L_{2B} = 32, L_{3A} = 15, L_{3B} = 15, S_1 = 0.5, S_2 = 3.0, S_2 = 1.5, and S_4 = 0.5. The dual-band BPF insertion loss/fractional bandwidth was 0.48 dB/7.71% and 0.35 dB/12.37% at 1.82 and 2.58 GHz, respectively. Figure 5C,D show photographs of the fabricated dual-band BPF and comparisons of the simulated and measured results, respectively. Moreover, Table 1 shows comparison with some previous dual-band BPFs such as References 11-19.

The proposed method is validated by the good agreement between the simulated and measured results. Furthermore, Table 1 gives the performance comparison of the dual-band BPF with some previous works, from which it can be deduced that the proposed BPF structure can enable adjustment of the frequency, bandwidth, reflection coefficient, and isolation of each passband individually with convenience and robustness.

4 | CONCLUSIONS

We have successfully designed an independent dual-band bandpass filter with a highly controllable working frequency/frequency center, bandwidth, reflection coefficient, and isolation between the passbands. This performance can be obtained by applying the source-load coupling with a stub-block isolation structure. The proposed dual-band BPF was fabricated on an RT/Duroid 5880 substrate. Furthermore, this dual-band BPF achieved an insertion loss/fractional bandwidth of 0.48 dB/7.71% and 0.35 dB/12.37% at 1.82 and 2.58 GHz, respectively. The good agreement between the simulated and measured results validates the proposed method.

ACKNOWLEDGMENT

The study was supported by a grant from the Ministry of Research, Technology and Higher Education, Indonesian Government.

ORCID

Yus Rama Denny https://orcid.org/0000-0002-4418-0758

Teguh Firmansyah https://orcid.org/0000-0002-9000-9337

REFERENCES

[1] Lim K et al. A 65-nm CMOS 2 × 2 MIMO multi-band LTE RF transceiver for small cell base stations. *IEEE J Solid-State Circuits*. 2018;53(7):1960-1976. https://doi.org/10.1109/JSSC.2018.2824300.

[2] Shi J, Lin L, Chen JX, Chu H, Wu X. Dual-band bandpass filter with wide stopband using one stepped-impedance ring resonator with shorted stubs. *IEEE Microw Wirel Compon Lett.* 2014;24(7):442-444. https://doi.org/10.1109/LMWC.2014.2316259.

[3] Luo XH, Cheng X, Han JA, et al. Compact dual-band bandpass filter using defected SRR and irregular SIR. *Electron Lett.* 2019;55(8):463-465. https://doi.org/10.1049/el.2018.8032.

[4] Chen JX, Shao C, Shi J, Bao ZH. Multilayer independently controllable dualband bandpass filter using dual-mode slotted-patch resonator. *Electron Lett.* 2013;49(9):605-607. https://doi.org/10.1049/el.2013.0238.

[5] Wangshuxing I, Zhou D, Zhang D, Han S. Dual-band bandpass filter using loop resonator with independently-tunable passband. *Electron. Lett.* 2017;53(25):1655-1657. https://doi.org/10.1049/el.2017.2397.

[6] Firmansyah T, Praptodinoyo S, Wiryadinata R, et al. Dual-wideband band pass filter using folded cross-stub stepped impedance resonator. *Microw Opt Technol Lett.* 2017;59(11):2929-2934. https://doi.org/10.1002/mop.30848.

[7] Zhang H, Kang W, Wu W. Miniaturized dual-band SIW filters using E-shaped slotlines with controllable center frequencies. *IEEE Microw Wirel Compon Lett.* 2018;28(4):311-313. https://doi.org/10.1109/LMWC.2018.2811251.

[8] Ieu W, Zhou D, Zhang D, Lv D. Compact dual-mode dual-band HMSIW bandpass filters using source–load coupling with multiple transmission zeros. *Electron Lett.* 2019;55(4):210-212. https://doi.org/10.1049/el.2018.7694.

[9] Zhang R, Zhu L, Luo S. Dual-mode dual-band bandpass filter using a single slotted circular patch resonator. *IEEE Microw Wirel Compon Lett.* 2012;22(5):233-235. https://doi.org/10.1109/LMWC.2012.2192419.

[10] Xu LJ, Zhang G, Tang YM, Bo YM. Compact dual-mode dual-band bandpass filter with wide stopband for WLAN applications. *Electron Lett.* 2015;51(17):1372-1374. https://doi.org/10.1049/el.2015.1913.

[11] Wang LT, Xiong Y, Gong L, Zhang M, Li H, Zhao XJ. Design of dual-band bandpass filter with multiple transmission zeros using transversal signal interaction concepts. *IEEE Microw Wirel Compon Lett.* 2019;29(1):32-34. https://doi.org/10.1109/LMWC.2018.2884147.

[12] Pal B, Mandal MK, Dwari S. Varactor tuned dual-band bandpass filter with independently tunable band positions. *IEEE Microw Wirel Compon Lett.* 2019;29(4):255-257. https://doi.org/10.1109/LMWC.2019.2898725.

[13] Gómez-garcía R, Yang L. Selectivity-enhancement technique for dual-passband filters. *IEEE Microw Wirel Compon Lett.* 2019;29(7):2019-2021.

[14] J. X. Xu, X. Y. Zhang, and Y. Yang, High-Q-factor dual-band bandpass filter and filtering switch using stub-loaded coaxial resonators. 2019 IEEE MTT-S International Wireless Symposium, IWS 2019: Proceedings, pp. 2019–2021, 2019, doi: https://doi.org/10.1109/IEEE-IWS.2019.8803878.

[15] Tan Z, Lu QY, Chen JX. Differential dual-band filter using ground Bar-loaded dielectric strip resonators. *IEEE Microw Wirel Compon Lett.* 2020;30(2):148-151. https://doi.org/10.1109/LMWC.2019.2957980.

[16] Z. Cao, X. Bi, and Q. Xu, Compact reflectionless dual-band BPF by reused quad-mode resonator, Paper presented at: 2019 Computing Communications and IoT Applications, ComComAp 2019. pp. 184–186, 2019, doi: https://doi.org/10.1109/ComComAp46287.2019.9018772.

[17] Z. Qian, Design of a dual-band balanced SIW bandpass filter with high common-mode suppression, Paper presented at: 2019 International Applied Computational Electromagnetics Society Symposium, ACES 2019. pp. 12–13, 2019, doi: https://doi.org/10.23919/ACES48530.2019.9060581.

[18] Gorur AK. A dual-band Balun BPF using Codirectional Split ring resonators. *IEEE Microw Wirel Compon Lett.* 2020;1–4(1):10-13.

[19] S. I. Hugar, V. Mungurwadi, and J. S. Baligar, Dual band microstrip BPF with controlled wide and narrow pass bands. Paper presented at: 2019 10th International Conference on Computing, Communication, and Networking Technologies, ICCCNT 2019. pp. 11–14, 2019, doi: https://doi.org/10.1109/ICCCNT45670.2019.8944399.

How to cite this article: Denny YR, Firmansyah T. A highly independent and controllable dual-band bandpass filter based on source-load coupling with stub-block isolation structure. *Microw Opt Technol Lett.* 2020;1–7. https://doi.org/10.1002/mop.32696